Effect of Elastic Anisotropy on Surface Pattern Evolution of Epitaxial Thin Films

Yaoyu Pang[$] and Rui Huang[*]

Department of Aerospace Engineering and Engineering Mechanics

University of Texas, Austin, Texas 78712

ABSTRACT

Stress-induced surface instability and evolution of epitaxial thin films leads to formation of a variety of self-assembled surface patterns with feature sizes at micro- and nanoscales. The anisotropy in both the surface and bulk properties of the film and substrate has profound effects on the nonlinear dynamics of surface evolution and pattern formation. Experimentally it has been demonstrated that the effect of anisotropy strongly depends on the crystal orientation of the substrate surface on which the film grows epitaxially. In this paper we develop a nonlinear model for surface evolution of epitaxial thin films on generally anisotropic crystal substrates. Specifically, the effect of bulk elastic anisotropy of the substrate on epitaxial surface pattern evolution is investigated for cubic germanium (Ge) and SiGe films on silicon (Si) substrates with four different surface orientations: Si(001), Si(111), Si(110), and Si(113). Both linear analysis and nonlinear numerical simulations suggest that, with surface anisotropy neglected, ordered surface patterns form under the influence of the elastic anisotropy, and these surface patterns clearly reflect the symmetry of the underlying crystal structures of the substrate. It is concluded that consideration of anisotropic elasticity reveals a much richer dynamics of surface pattern evolution as compared to isotropic models.

Keywords: Surface pattern; Epitaxial film; Anisotropic elasticity

[$] Now at Texas Instruments, 13536 North Central Expressway, Mail Stop 940, Dallas, Texas 75243.

[*] Corresponding author. Tel: 1-512-471-7558; fax: 1-512-471-5500; email: ruihuang@mail.utexas.edu.

1. Introduction

A large variety of surface patterns have been observed in epitaxially grown crystal thin films. In the most common growth mode, Stranski-Krastanov (SK) mode, a transition from two-dimensional (2D) growth of a nominally flat film to three-dimensional (3D) growth of coherent islands occurs above a critical mean film thickness (Eaglesham and Cerullo, 1990). The transition has been understood as a result of stress induced surface instability of the epitaxial film. In general, a macroscopically planar surface of a stressed solid is thermodynamically unstable, with a tendency to relax the elastic strain energy by surface roughening (Asaro and Tiller, 1972; Grinfeld, 1986; Srolovitz, 1989). An epitaxial film is inherently stressed due to mismatch of crystal lattices between the film and the substrate, thus unstable. The critical thickness for the 2D-3D transition during the SK growth has been predicted by introducing a wetting potential in competition with the strain energy and surface energy (Tekalign and Spencer, 2004; Pang and Huang, 2006). Subsequent growth of 3D islands exhibits intriguingly rich dynamics with shape transition and self organization (Medeiros-Ribeiro et al., 1998; Floro et al., 1999; Ross et al., 1999). The potential to grow nanoscale islands (quantum dots or nanocrystals) by self assembly has motivated extensive studies since early 1990s, with an objective to develop novel applications in optoelectronics and nanoelectronics (Brunner, 2002). Practical applications often require controllable synthesis of ordered surface structures with uniform feature sizes and long-range spatial organizations. Despite tremendous efforts with both experimental and modeling progresses in recent years, many questions remain open for the growth and evolution dynamics of epitaxial surfaces, in particular, regarding the conditions under which ordered surface patterns form as

well as the underlying mechanisms that control the size and ordering of self-assembled surface structures (e.g., quantum dots and nanowires).

In complement with experimental investigations, modeling and simulations have significantly enhanced understanding of the surface evolution dynamics and the underlying mechanisms. Different modeling approaches have been developed to simulate surface evolution and self assembly of quantum dots, such as kinetic Monte Carlo simulations (Meixner et al., 2001; Lam et al., 2002; Zhu et al., 2007) and phase-field modeling (Kassner et al., 2001; Ni et al., 2005; Seol et al., 2005). Surface differential equation based approaches have been developed for theoretical studies (Spencer et al., 1993; Chiu, 1999; Zhang and Bower, 1999; Shenoy and Freund, 2002), with well-posed foundation in relevant surface physics (e.g., thermodynamics, kinetics, and mechanics), relatively simple mathematical form, and yet nontrivial nonlinear solutions. Derived from a general framework of nonequilibrium thermodynamics, the governing equation for the surface morphology of an epitaxial thin film is typically written with the time evolution of the local film thickness on one side and a surface Laplacian of the chemical potential on the other; a flux term may be included to simulate growth during deposition, but often ignored for surface evolution during annealing. The chemical potential of a solid surface in general includes contributions from surface energy and elastic strain energy. For epitaxial thin films (thickness typically less than 100 nm), a thickness-dependent potential term is added to account for the interfacial interaction that leads to the 2D-3D transition and the formation of a thin wetting layer during the SK growth (Spencer, 1999). The competition among the three energy terms defines a thermodynamic configurational force that drives evolution of surface morphology and

formation of self-assembled patterns, a dynamic process kinetically facilitated by atomic diffusion on the surface at elevated temperatures during deposition or annealing.

Most of the previous studies have assumed isotropic elasticity for the film and the substrate. This assumption however contradicts the crystalline nature in essentially all epitaxial systems. While the anisotropic elasticity may not be critically important for the basic understanding of the surface instability, it is expected to play a significant role in the ordering of surface patterns over long term evolution (Meixner et al., 2001; Ni et al., 2005; Liu et al., 2006). Previously, Shenoy and Freund (2002) developed an anisotropic solution to the first order of the surface slope, by using an elastic half-space Green's function. In the present study, a nonlinear solution is obtained by the method of Fourier transform for a generally anisotropic half space, to the second order of the surface slope. With this solution, the effect of elastic anisotropy of the substrate on surface pattern evolution can be theoretically investigated for both the linear and nonlinear regimes.

A large number of modeling works have assumed isotropic surface energy for epitaxial surface evolution. While more complex forms of surface energy accounting for crystal surface anisotropy and surface stress have been developed in order to understand the size and shape of self-assembled islands (e.g., Chiu, 1999; Zhang and Bower, 2001; Shenoy and Freund, 2002; Savina et al., 2003 and 2004), their applications have been hindered by the very limited knowledge of the additional parameters from either experiments or first-principle models. To focus on the effect of bulk elastic anisotropy, in the present study we take the surface energy to be isotropic and independent of strain, leaving combination and competition of various anisotropy effects for future studies.

The characteristic 2D-3D transition of Stranski-Krastanov growth along with the presence of a thin wetting layer underlying self-assembled islands at the later stage suggests that a critical thickness exists, below which the flat film surface is stabilized. Different physical origins and modeling approaches of the critical thickness have been proposed (e.g., Kukta and Freund, 1997; Spencer, 1999). A general discussion on the effect of the wetting potential on surface instability and pattern evolution dynamics was presented by Golovin et al. (2003). For the present study, we adopt the wetting potential derived from a surface energy transition-layer model (Spencer, 1999).

The remainder of this paper is organized as follows. Section 2 presents a general formula of nonlinear, anisotropic evolution equation. Section 3 develops a solution procedure for the generally anisotropic elasticity problem, up to the second order of the surface slope. Section 4 performs a linear analysis of the surface evolution, and Section 5 describes the numerical method for nonlinear simulations. In Section 6, results for specific epitaxial systems are presented, and the effect of elastic anisotropy on surface pattern evolution is discussed. Section 7 concludes with a remark on the extension of the present model.

2. Anisotropic, Nonlinear Evolution Equation

Previously, we developed a nonlinear equation for surface evolution assuming isotropy in both bulk elasticity and surface properties (Pang and Huang, 2006). Here, we extend the model for epitaxial systems with general elastic anisotropy. Due to the nature of crystalline structures, real epitaxial systems are all anisotropic, and the effect of anisotropy varies with the type of the crystal structure as well as the crystal orientation of the surface.

Figure 1 schematically illustrates an epitaxial system, with a single-crystal thin film on a thick crystal substrate. The film is stressed due to mismatch in the crystal lattices between the film and the substrate, and the rough film surface is described by a thickness profile function, $x_3 = h(x_1, x_2, t)$, with h_0 being the mean film thickness. An epitaxial coordinates are set up such that $x_3 = 0$ at the film/substrate interface. On the other hand, the natural crystal coordinates, denoted by (x'_1, x'_2, x'_3), may or may not align with the epitaxial coordinates, depending on the surface orientation of the substrate.

The chemical potential on the film surface includes contributions from surface energy, elastic strain energy, and a wetting potential, namely

$$\mu = \Omega\left(U_E + U_S + U_W\right). \tag{1}$$

where Ω is the atomic volume.

The gradient of the surface chemical potential drives surface diffusion. Assuming a linear kinetic law, the surface diffusion flux is

$$J_\alpha = -M_{\alpha\beta}\frac{\partial}{\partial x_\beta}\left(\mu\sqrt{1+h_\chi h_\chi}\right), \tag{2}$$

where $M_{\alpha\beta}$ represents a generally anisotropic surface mobility and $h_\beta = \partial h/\partial x_\beta$ is the local surface slope. The Greek indices, α, β, χ, take values 1 and 2 for the coordinates parallel to the film/substrate interface as illustrated in Fig. 1; a repeated Greek index implies summation over 1 and 2. Note that, in Eq. (2), the chemical potential is projected onto a plane parallel to the film/substrate interface before taking the gradient with respect to the in-plane coordinates. Assuming isotropic surface diffusion for the present study, we have $M_{\alpha\beta} = M_0\delta_{\alpha\beta}$, where M_0 is a constant mobility and $\delta_{\alpha\beta}$ is the Kronecker delta.

By mass conservation, the divergence of the surface flux leads to change of the local

thickness, namely

$$\frac{\partial h}{\partial t} = \Omega^2 M_{\alpha\beta} \frac{\partial^2}{\partial x_\alpha \partial x_\beta} \left[\left(U_E + U_S + U_W \right) \sqrt{1 + h_\chi h_\chi} \right]. \tag{3}$$

Equation (3) is a general form of anisotropic, nonlinear evolution equation. The elastic strain energy density at the surface, U_E, is to be determined by solving an anisotropic boundary value problem (see Section 3). In general, the contribution from surface energy, U_S, is anisotropic and depends on the surface deformation through surface stresses (e.g., Chiu, 1999; Zhang and Bower, 2001; Shenoy and Freund, 2002). For the present study, to focus on the effect of bulk elastic anisotropy, we assume an isotropic surface energy independent of the surface deformation, and thus

$$U_S = -\kappa\gamma\,, \tag{4}$$

where γ is the surface energy density and κ is the local mean curvature of the surface, i.e.

$$\kappa = \frac{\left(1 + h_\alpha h_\alpha\right) h_{\beta\beta} - h_\alpha h_\beta h_{\alpha\beta}}{\left(1 + h_\alpha h_\alpha\right)^{3/2}}\,. \tag{5}$$

To account for the wetting interaction, Spencer (1999) proposed a thickness-dependent surface energy:

$$\gamma(h) = \frac{1}{2}\left(\gamma_s + \gamma_f\right) - \frac{1}{\pi}\left(\gamma_s - \gamma_f\right) \arctan\left(\frac{h}{b}\right), \tag{6}$$

where γ_f and γ_s are the surface energy density constants of the film and the substrate, respectively, and b is a parameter controlling the thickness of the transition layer at the interface. The transition-layer model naturally leads to an isotropic wetting potential

$$U_W = -\frac{\gamma_s - \gamma_f}{\sqrt{1 + h_\alpha h_\alpha}} \frac{b}{\pi(b^2 + h^2)}\,. \tag{7}$$

It has been shown that the wetting potential plays a critical role in the surface evolution for

ultrathin films and the formation of a wetting layer (Savina et al., 2004).

3. Anisotropic Elasticity Solution

The stress field in the epitaxial system, σ_{ij}, satisfies the traction-free boundary condition at the film surface ($x_3 = h$):

$$\sigma_{ij} n_j = 0, \tag{8}$$

with a unit vector of the surface normal given by

$$n_\alpha = \frac{-h_\alpha}{\sqrt{1+h_\beta h_\beta}}, \qquad n_3 = \frac{1}{\sqrt{1+h_\beta h_\beta}}. \tag{9}$$

The undulating surface of the film leads to a nonlinear boundary value problem, whereas the materials (film and substrate) are subject to infinitesimal deformation and regarded as linearly elastic.

Consider a reference state with a film of uniform thickness, $h = h_0$. The stress field at the reference state is uniform, with nonzero in-plane components in the film: $\sigma_{11}^{(0)}$, $\sigma_{12}^{(0)}$ and $\sigma_{22}^{(0)}$, and $\sigma_{33}^{(0)} = \sigma_{31}^{(0)} = \sigma_{32}^{(0)} = 0$, while the substrate is stress free. The magnitude of the film stress depends on the lattice mismatch and the elastic moduli of the film; both can be anisotropic in general. The strain energy density at the flat surface of the reference state is a constant:

$$U_E^{(0)} = \frac{1}{2}\sigma_{\alpha\beta}^{(0)}\varepsilon_{\alpha\beta}^{(0)}, \tag{10}$$

where $\varepsilon_{\alpha\beta}^{(0)}$ is the in-plane strain in the epitaxial film due to lattice mismatch. The relationship between the mismatch strain and the mismatch stress is given by Hooke's law and depends on the crystal orientation of the epitaxial system (Caro and Tapfer, 1993). It is often convenient to set up the in-plane coordinates to align with the principal directions of the

mismatch stress so that the shear component $\sigma_{12}^{(0)} = 0$.

As the film surface evolves, the stress field changes along with the surface morphology, dictated by the boundary condition. Due to the moving boundary and the nonlinearity of the surface normal, the elasticity problem can only be solved numerically. Previously, an asymptotic approach was developed for isotropic systems (Pang and Huang, 2006). Here we extend the approach for generally anisotropic systems. First, the stress field is expressed in form of a series expansion:

$$\sigma_{ij} = \sigma_{ij}^{(0)} + \sigma_{ij}^{(1)} + \sigma_{ij}^{(2)} + \cdots, \tag{11}$$

where $\sigma_{ij}^{(0)}$ is the stress at the reference state, $\sigma_{ij}^{(1)}$ represents a linear perturbation, and $\sigma_{ij}^{(2)}$ is the leading nonlinear term of the stress field (second-order perturbation). In principle, successively higher order terms can be included.

By substituting Eq. (11) into the boundary condition (8) and keeping only the first-order terms, we obtain the reduced boundary condition for the first-order stress field:

$$\sigma_{3\alpha}^{(1)} = \sigma_{\alpha\beta}^{(0)} h_\beta \quad \text{and} \quad \sigma_{33}^{(1)} = 0. \tag{12}$$

Similarly, for the second-order stress field, the boundary conditions are:

$$\sigma_{3\alpha}^{(2)} = \sigma_{\alpha\beta}^{(1)} h_\beta \quad \text{and} \quad \sigma_{33}^{(2)} = \sigma_{\alpha\beta}^{(0)} h_\alpha h_\beta. \tag{13}$$

Both the reduced boundary conditions should be applied at the film surface, i.e., $x_3 = h$ (Fig. 1). A couple of approximations are adopted here to solve the boundary value problems. First, it is assumed that the film thickness has relatively slow variation along the in-plane directions and the boundary conditions on the undulating surface can be approximated by those on a flat surface with the mean film thickness (i.e., $x_3 = h_0$). As will be shown later from numerical simulations, the surface pattern usually has a characteristic length (e.g.,

wavelength for a periodic pattern) much greater than the undulation amplitude. From experimental observations, the diameter of self-assembled quantum dots is typically 1-2 orders of magnitude greater than their height, thus justifying the small-slope approximation. The second approximation is to take the film and the substrate together as a homogeneous half space. When the elastic properties for the film and the substrate are similar, such as a SiGe film on a Si substrate, the substrate property is used for the half space as a reasonable approximation. It has also been shown that, at the limit of very thin films, the elastic deformation at the film surface is predominantly controlled by the substrate elasticity (Tekalign and Spencer, 2004). Therefore, in the following, the surface displacements corresponding to the first and second-order stress fields are determined approximately by solving respective homogeneous half-space problems with the boundary conditions (12) and (13). Here, the effect of substrate elasticity is taken into account in the calculation of the surface displacement and strain, while the elastic property of the film is used in calculating the film stresses (e.g., $\sigma_{\alpha\beta}^{(0)}$). As a result, two origins of the elastic anisotropy can be identified, one due to the mismatch stress as related to the elastic anisotropy of the film and the other due to the anisotropic substrate.

The generally anisotropic, linear elastic half-space problem is solved by a Fourier transform method as detailed in Appendix A. The solution gives a relationship between the surface tractions as specified in the reduced boundary conditions and the surface displacements, in terms of their Fourier transforms, namely

$$\hat{u}_j^{(n)}(k_1,k_2) = Q_{ji}(k_1,k_2)\hat{\sigma}_{3i}^{(n)}. \tag{14}$$

where k_1, k_2 are the coordinates in the Fourier space (i.e., components of the wave vector),

Q_{ji} is a compliance matrix that depends on the elastic property of the substrate as given in Eq. (A.13), and $n = 1,2$ for the first and second-order solutions, respectively.

With the series expansion of the stress field in Eq. (11), the strain energy density at the film surface can be expressed in a similar form:

$$U_E = U_E^{(0)} + U_E^{(1)} + U_E^{(2)} + \cdots, \tag{15}$$

where $U_E^{(0)}$ is the strain energy density at the reference state as given in Eq. (10), and

$$U_E^{(1)} = \sigma_{\alpha\beta}^{(0)} \frac{\partial u_\alpha^{(1)}}{\partial x_\beta}, \tag{16}$$

$$U_E^{(2)} = \sigma_{\alpha\beta}^{(0)} \frac{\partial u_\alpha^{(2)}}{\partial x_\beta} + \frac{1}{2}\sigma_{\alpha\beta}^{(1)} \frac{\partial u_\alpha^{(1)}}{\partial x_\beta} + \sigma_{\alpha\beta}^{(0)} h_\beta \left(\frac{\partial u_3^{(1)}}{\partial x_\alpha} + \frac{\partial u_\alpha^{(1)}}{\partial x_3} \right). \tag{17}$$

The term $U_E^{(1)}$ is to the first order of surface undulation, and $U_E^{(2)}$ is to the second order as the leading nonlinear term; the higher order terms for the strain energy density are truncated for the present study.

4. Linear Analysis

Substitution of Eqs. (4), (7), and (15) into Eq. (3) leads to a nonlinear evolution equation. By keeping the first-order terms only, a linearized form of the evolution equation is obtained:

$$\frac{\partial h}{\partial t} = \Omega^2 M_0 \frac{\partial^2}{\partial x_\kappa \partial x_\kappa} \left[\sigma_{\alpha\beta}^{(0)} \frac{\partial u_\alpha^{(1)}}{\partial x_\beta} - \gamma_0 h_{\alpha\alpha} + \frac{2h_0 b(\gamma_s - \gamma_f)}{\pi(b^2 + h_0^2)^2} h \right], \tag{18}$$

where $\gamma_0 = \gamma(h_0)$ is the surface energy density at the mean film thickness.

Fourier transform of Eq. (18) leads to

$$\frac{\partial \hat{h}}{\partial t} = s(k_1, k_2)\hat{h}, \tag{19}$$

where

$$s(k_1,k_2)=\Omega^2 M_0 k^2\left[k_\alpha k_\beta Q_{\chi\kappa}\sigma^{(0)}_{\alpha\chi}\sigma^{(0)}_{\beta\kappa}-\gamma_0 k^2-\frac{2h_0 b(\gamma_s-\gamma_f)}{\pi(b^2+h_0^2)^2}\right]. \tag{20}$$

Integration of Eq. (19) over time gives that

$$\hat{h}(k_1,k_2,t)=A_0\exp\left[s(k_1,k_2)t\right], \tag{21}$$

where A_0 is the initial amplitude of the Fourier component, and s is the growth rate. The dependence of the growth rate on the wave numbers dictates the growth dynamics at the early stage of surface evolution, as shown in Fig. 2 for specific epitaxial systems. Discussions of the evolution dynamics are postponed till Section 6.

For an isotropic system with an equi-biaxial mismatch stress (i.e., $\sigma^{(0)}_{11}=\sigma^{(0)}_{22}=\sigma_0$ and $\sigma^{(0)}_{12}=0$), the growth rate becomes

$$s(k_1,k_2)=\Omega^2 M_0 k^2\left[\frac{2(1-\nu_s^2)}{E_s}\sigma_0^2 k-\gamma_0 k^2-\frac{2h_0 b(\gamma_s-\gamma_f)}{\pi(b^2+h_0^2)^2}\right], \tag{22}$$

where E_s and ν_s are Young's modulus and Poisson's ratio of the isotropic substrate. The first two terms in the bracket of Eq. (22) represent a competition between the elastic strain energy and the surface energy: the former drives growth of surface undulation and the latter drives negative growth or flattening of the surface. This competition defines a length scale and a time scale (Pang and Huang, 2006):

$$L=\frac{\gamma_f E_s}{2(1-\nu_s^2)\sigma_0^2}\quad\text{and}\quad\tau=\frac{\gamma_f^3 E_s^4}{16(1-\nu_s^2)^4\Omega^2 M_0\sigma_0^8}. \tag{23}$$

Similar length and time scales can be defined for generally anisotropic systems. For the present study, we set

$$L=\frac{\gamma_f \overline{E}_s}{2\left(\widetilde{E}_f\bar{\varepsilon}_m\right)^2}\quad\text{and}\quad\tau=\frac{\gamma_f^3\overline{E}_s^4}{16\Omega^2 M_0\left(\widetilde{E}_f\bar{\varepsilon}_m\right)^8}, \tag{24}$$

where $\bar{\varepsilon}_m=\frac{1}{2}\left(\varepsilon^{(0)}_{11}+\varepsilon^{(0)}_{22}\right)$ is the mean mismatch strain, $\overline{E}=C_{11}-C_{12}^2/C_{11}$ is the effective

plane-strain modulus, and $\widetilde{E} = C_{11} + C_{12} - 2C_{12}^2 / C_{11}$ the effective biaxial modulus. The subscripts *s* and *f* denote the substrate and film, respectively. The effective moduli are defined such that the scales in Eq. (24) recover those in Eq. (23) for an isotropic system.

The third term in the bracket of Eq. (20) or (22) represents the effect of wetting on the initial growth, which sets a critical thickness. For an isotropic system, we obtained that (Pang and Huang, 2006)

$$h_c = 2L\left(\frac{(\gamma_s - \gamma_f)b}{\pi\gamma_f L}\right)^{1/3}, \tag{25}$$

where $\gamma_s > \gamma_f$ has been assumed as a necessary condition for the film to wet the substrate surface. If the mean film thickness, $h_0 < h_c$, the surface is stable without roughening, while the surface becomes unstable when $h_0 > h_c$. This is consistent with the well-known 2D-3D transition in the Stranski-Krastanov growth of epitaxial films. Similarly, the critical thickness for an anisotropic system can be determined, taking the form

$$h_c = \eta L\left(\frac{(\gamma_s - \gamma_f)b}{\pi\gamma_f L}\right)^{1/3}, \tag{26}$$

where the coefficient η depends on the elastic anisotropy of the substrate and will be discussed in Section 6.

5. Numerical Simulations

By keeping up to the second-order terms for the elastic strain energy and surface curvature, we obtain a nonlinear evolution equation

$$\frac{\partial h}{\partial t} = \Omega^2 M_0 \frac{\partial^2}{\partial x_\kappa \partial x_\kappa}\left[\sigma_{\alpha\beta}^{(0)}\frac{\partial u_\alpha^{(1)}}{\partial x_\beta} + U_E^{(2)} + \frac{1}{2}U_E^{(0)}h_\alpha h_\alpha - \gamma h_{\alpha\alpha} - \frac{b(\gamma_s - \gamma_f)}{\pi(b^2 + h^2)}\right]. \tag{27}$$

A spectral method is employed for numerical simulations, similar to the previous study

for isotropic systems (Pang and Huang, 2006). Briefly, Fourier transform of Eq. (27) takes the generic form

$$\frac{\partial \hat{h}}{\partial t} = s(k_1, k_2)\hat{h} + \Phi(\hat{h}), \tag{28}$$

where $\Phi(\hat{h})$ represents the combination of all the nonlinear terms. A semi-implicit algorithm is then used to integrate Eq. (28) over time, namely

$$\hat{h}(k_1, k_2, t + \Delta t) = \frac{\hat{h}(k_1, k_2, t) + \Phi(\hat{h}; k_1, k_2, t)\Delta t}{1 - s(k_1, k_2)\Delta t}, \tag{29}$$

where Δt is the time increment at each step. Similar numerical methods have been developed for simulations of self-assembled surface monolayers (Lu and Suo, 2002) and evolution of wrinkle patterns (Huang and Im, 2006).

A brief description of the simulation procedures follows. For a given epitaxial system, the mean film thickness and the mismatch strain are specified. With the anisotropic elastic moduli of the substrate, the compliance matrix, Q_{ij}, is calculated following the steps in Appendix A. Then, taking a randomly generated perturbation of small amplitude to the mean film thickness as the initial condition, the surface evolution is simulated by updating the thickness profile over a number of time steps. For each time step, we compute the Fourier transform of the current thickness profile, $\hat{h}(k_1, k_2, t)$, by the Fast Fourier Transform (FFT) method. In the reciprocal Fourier space, the linear quantities (e.g., $ik_\alpha \hat{h}$, $\hat{u}_i^{(1)} = ik_\beta Q_{i\alpha}\sigma_{\alpha\beta}^{(0)}\hat{h}$, and $ik_\beta \hat{u}_i^{(1)}$) are computed by simple multiplications at each grid point (Fourier component). Next, we obtain corresponding quantities in the real space (e.g., h_α, $u_i^{(1)}$, and $\frac{\partial u_i^{(1)}}{\partial x_\beta}$) by inverse FFT (IFFT), and compute the nonlinear terms, such as $\sigma_{3\alpha}^{(2)} = \sigma_{\alpha\beta}^{(1)} h_\beta$,

$\sigma_{33}^{(2)} = \sigma_{\alpha\beta}^{(0)} h_\alpha h_\beta$, $\sigma_{\alpha\beta}^{(1)} \dfrac{\partial u_\alpha^{(1)}}{\partial x_\beta}$, $h_\alpha h_\alpha$, and $\gamma h_{\alpha\alpha}$, by simple multiplications at each grid point of the physical space. Then, we transform the nonlinear terms back into the Fourier space and update the Fourier transform of the thickness profile with $\hat{h}(k_1, k_2, t + \Delta t)$ by Eq. (29). The final thickness profile in the physical space is obtained by IFFT at the end of the simulation.

6. Results and Discussions

Our previous study (Pang and Huang, 2006) has shown that the nonlinear evolution equation for isotropic systems predicts surface evolution and formation of randomly located circular islands on top of a thin wetting layer. By considering anisotropic mismatch stresses in an otherwise isotropic system, we have revealed a symmetry breaking and bifurcation of surface patterns (Pang and Huang, 2007). In the present study, to elucidate the effect of elastic anisotropy, we consider specific epitaxial systems with anisotropic elastic properties for both the films and the substrates. Cubic Ge and SiGe films on Si substrates of various surface orientations are studied in detail, and the effects of film thickness and Ge concentration are discussed.

6.1 Ge/SiGe films on Si

Both Si and Ge have cubic crystalline structures, and they form completely miscible solid solution, SiGe, over the entire range of Ge concentration (Fitzgerald, 1996). The elastic moduli of Si and Ge are listed in Table I, referring to their natural crystal coordinates (Freund and Suresh, 2003). By the rule of transformation for the elasticity tensor as outlined in Appendix B, the elastic constants with respect to the epitaxial coordinate for an arbitrary

surface orientation (see Fig. 1) can be obtained. The values of surface energy density for Si and Ge are also listed in Table I, for four surface orientations: (001), (111), (110), and (113). We note quite a scattering in the reported surface energy values obtained from experiments and theoretical calculations, which vary significantly with specific surface conditions such as surface relaxation, reconstruction, and hydrogenation (Stekolnikov et al., 2002 and 2003). For simplicity, we use the values of unrelaxed surfaces in the present study.

The elastic moduli of a SiGe alloy are obtained by a linear interpolation between those of Si and Ge (Fitzgerald, 1996), namely

$$C_{ijkl}^{SiGe} = (1-x)C_{ijkl}^{Si} + xC_{ijkl}^{Ge}, \tag{30}$$

where x is Ge concentration ($0 \le x \le 1$). Similarly, we take the surface energy density of SiGe as

$$\gamma_{SiGe} = (1-x)\gamma_{Si} + x\gamma_{Ge}. \tag{31}$$

Experiments have shown that the lattice constant of SiGe is closely matched with a simple linear interpolation between Si and Ge (Fitzgerald, 1996), i.e.,

$$a_{SiGe} = (1-x)a_{Si} + xa_{Ge}, \tag{32}$$

where $a_{Si} = 0.5428\,\text{nm}$ and $a_{Ge} = 0.5658\,\text{nm}$. Consequently, the lattice mismatch between an epitaxial SiGe film and its Si substrate induces an equi-biaxial compressive strain in the film:

$$\varepsilon_{11}^{(0)} = \varepsilon_{22}^{(0)} = \varepsilon_m = \frac{a_{Si} - a_{SiGe}}{a_{SiGe}} \approx -0.042x. \tag{33}$$

Note that the mismatch strain is independent of either the crystal orientation of the epitaxial surface or the selection of the in-plane coordinate axes. On the other hand, the mismatch stress in general varies with both due to anisotropy in the elastic moduli.

The only parameter that remains to be determined in the present model is the thickness b for the transition of surface energy at the film/substrate interface. It is noted that the critical thickness as predicted from the linear analysis in Eq. (26) explicitly depends on b and can be compared with experimentally determined critical thickness as a way to estimate the value of b. For epitaxial growth of Ge on Si(001), experimental observations suggested that the critical thickness for the 2D-3D transition is around 0.7-1.0 nm (3-5 monolayers) (Eaglesham and Cerullo, 1990; Abstreiter et al., 1996). By taking $h_c = 0.7$ nm, we obtain $b = 0.02$ nm for Ge on Si(001). For SiGe films, both the critical thickness and the transition layer thickness may vary with the substrate orientation and Ge concentration. In the present study, we use the same transition layer thickness for different substrate orientations, but increase the thickness b for SiGe films as the Ge concentration decreases.

In the numerical simulations presented below, we normalize the evolution equation using the length and time scales defined in Eq. (24) and discretize the computational cell of size 100 ×100 into a 128 by 128 grid with a periodic boundary condition. To compare the results for different crystal orientations, the length scale on the Si(001) substrate is used for all calculations. For a pure Ge film (x = 1), the length scale is: $L = 3.83$ nm. The length scale increases dramatically for SiGe films as the Ge concentration decreases.

6.2 Early-stage evolution

Starting from a nearly flat film surface, the evolution dynamics at the early stage can be understood based on the linear analysis presented in Section 4. First, the growth rate of each Fourier component as a function of its wave vector, as given in Eq. (20), dictates the stability

and the fastest growing modes. Figure 2 plots the contours of the growth rate in the plane of (k_1, k_2) for Ge films of a mean thickness, $h_0 = 0.2L$, on Si substrates; only positive growth rates are shown in the contours. For the Ge/Si(001) epitaxy (Fig. 2a), the growth rate is positive in a diamond shaped region, with four peaks symmetrically located on the k_1 and k_2 axes. This predicts the fastest growing modes at the early stage, with the wave vectors along the [100] and [010] directions. Apparently, the elastic anisotropy of the cubic crystal breaks the rotational symmetry that is characteristic of surface evolution in isotropic systems (Pang and Huang, 2006). As will be shown later by numerical simulations, the break of symmetry eventually leads to ordered surface patterns as opposed to the lack of ordering in the isotropic systems.

While the Si(001) has been the most commonly used substrate, here we show that the surface evolution dynamics can be drastically different for epitaxial films on other orientations of Si. For Ge/Si(111) epitaxy (Fig. 2b), the contours of the growth rate are nearly concentric circles, similar to that for isotropic systems. This is not surprising as we notice that the triangular lattice structure on the Si(111) plane indeed leads to macroscopically isotropic in-plane elastic properties. As a result, the early-stage surface evolution on Si(111) resembles that in an isotropic system, with no preferred directions for the fastest growing modes. For Ge/Si(110) epitaxy (Fig. 2c), the contour plot shows two peaks of the growth rate on the axis parallel to the $[\bar{1}10]$ direction. This predicts growth of stripe patterns parallel to the [001] direction on the (110) surface. For Ge/Si(113) epitaxy (Fig. 2d), there are four peaks in the growth rate contour, corresponding to wave vectors in two directions with angles $\pm 31^\circ$ off the $[\bar{3}\bar{3}2]$ direction on the (113) surface. This is similar to the bifurcation of the growth

mode due to anisotropic mismatch stresses in an otherwise isotropic system (Pang and Huang, 2007). Here, however, the bifurcation is a result of the combined effect due to anisotropic mismatch stress and anisotropic substrate elasticity.

Figure 3 plots the peak growth rate and the corresponding wavelength ($\lambda = 2\pi / k$) versus the mean film thickness for Ge on Si substrates. For each substrate orientation, there exists a critical thickness, below which the maximum growth rate is negative and thus the film is stable with a flat surface. The critical thickness varies slightly with the substrate orientation. For Ge on Si(001), $h_c = 0.18L \approx 0.7nm$, which is about five monolayers thick. Using the same transition layer thickness $b = 0.02$ nm, the predicted critical thicknesses for the other orientations are smaller: $h_c = 0.10L \approx 0.4nm$ for both Si (111) and Si (110), and $h_c = 0.14L \approx 0.55nm$ for Si (113). For a film with the mean thickness greater than the critical thickness, the maximum growth rate becomes positive and the flat film surface is unstable. The growth rate increases with the mean film thickness, and saturates for relatively thick films. Similar behavior was predicted for isotropic systems (Pang and Huang, 2006), as a result of the wetting effect: the wetting potential suppresses the surface instability for ultrathin films, but has little effect on the early-stage evolution for relatively thick films. Figure 3b shows the similar trend for the wavelength of the fastest growing mode at the early stage. Only beyond the critical thickness, does there exist a dominant wavelength, which decreases with the mean film thickness and saturates for relatively thick films.

Comparison of the normalized growth rates and wavelengths for different crystal orientations of the Si substrates shows an interesting trend. With same mean film thicknesses, the Ge/Si(001) epitaxial system is the most stable among the four orientations, with the

lowest growth rate and the longest wavelength. The epitaxial surfaces are increasingly unstable in the order of Ge/Si(113), Ge/Si(111), and Ge/Si(110). Remarkably, while the (111) surfaces of both Si and Ge have the lowest surface energy, the epitaxial Ge(111) surface on Si(111) substrate is less stable compared to the (001) and (113) surfaces. Apparently, the stability of an epitaxial surface is not solely controlled by the surface energy. It should be noted that the time scale τ used to normalize the growth rate may vary with the surface orientation through the anisotropic surface energy γ_f and diffusivity M_0, $\tau \sim \gamma_f^3 / M_0$, as defined in Eq. (24). Moreover, the surface diffusivity is also sensitive to the temperature as well as other growth conditions. Experimentally, the growth rates of Ge islands on Si substrates at 700°C were observed to increase in the order of (111), (110) and (001) (Vescan, 2002).

For epitaxial SiGe alloy films, the evolution dynamics is similar except for the length and time scales. As defined in Eq. (24), the length scale depends on the mismatch strain, elastic moduli, and surface energy density, all of which vary with the Ge concentration x as given in Eqs. (30)-(33). The effects of concentration-dependent elastic moduli and surface energy density on the length scale have been neglected in previous theoretical studies (Srolovitz, 1989), leading to a simple scaling for the length, $L \propto 1/x^2$. However, as pointed out by Dorsch et al. (1998A), this scaling has to be corrected by considering the compositional dependence of the elastic moduli among other possible causes. The length scale plays an important role in the determination of the critical thickness and the dominant wavelength at the early stage of surface evolution. As given in Eq. (26), the critical thickness roughly scales with the length L. Figure 4 plots the critical thickness as a function of the Ge concentration

for epitaxial SiGe films on Si substrates. Here, the transition layer thickness is taken to be: $b = 0.005L$, where L varies with x. Clearly, the critical thickness increases rapidly as the Ge concentration decreases, approaching infinity as $x \to 0$ for stable, homoepitaxial growth of Si. A few experimental data (Abstreiter et al., 1996; Osten et al., 1994; Floro et al., 1999) are included in Fig. 4 for comparison, all for SiGe films on Si(001) substrates. The agreement between the present model predictions and the experimental data is reasonably good for a wide range of Ge concentration.

Figure 5 plots the wavelength of the fastest growing mode at the early stage of surface evolution in epitaxial SiGe films as a function of Ge concentration. The film thickness is set to be 100 nm. As shown in Fig. 3b, the wavelength becomes independent of the film thickness for relatively thick films. This wavelength scales linearly with the length scale L, but varies slightly with the crystal orientations of the substrates. It is noted that, while the wavelength is well above 1 μm for SiGe films with low Ge concentration (e.g., $x < 0.2$), the dominant wavelength is well below 100 nm for Ge-rich films (e.g., $x > 0.8$). The large variation in the length scale thus offers a potential approach to tunable surface patterns. Experimentally, surface rippling at the early-stage of evolution have been observed for epitaxial SiGe films on Si (001) substrates (Cullis et al., 1994; Jesson et al., 1997; Dorsch et al., 1998B; Gao and Nix, 1999). In particular, Dorsch et al. (1998B) presented a detailed study on the morphological evolution of SiGe films of low Ge concentration ($0.05 \le x \le 0.15$), and their measurements for the wavelengths of the ripple patterns at the early stage are included in Fig. 5. It is noted that the predicted wavelength is consistently greater than the experimental data, approximately by a factor of two.

6.3 Long-term evolution

Beyond the linear regime, long-term evolution of epitaxial surface morphology by numerical simulations are shown in Figs. 6-9, for Ge films on Si(001), Si(111), Si(110), and Si(113) substrates, respectively. The mean film thickness for the simulations is $h_0 = 1.2h_c$, with slightly different critical thicknesses for different substrate orientations. All simulations start from a flat surface with a randomly generated initial perturbation of a small amplitude, $0.0001L$. As predicted by the linear analysis, surface evolution at the early stage is dominated by the fastest growing modes. On the Si(001) substrate (Fig. 6), the film surface first evolves into shallow ripples in both [100] and [010] directions. The initially interconnected ridges then break up into chains of islands. These islands are well organized, eventually forming a cubic array, like a macroscopic replicate of the underlying cubic crystal structure. Apparently, the anisotropic elastic property effectively represents the cubic crystal structure and drives the ordering of the surface pattern. Experimentally, similar ordering of islands was observed in SiGe films with low Ge concentrations (Dorsch et al., 1998B; Gao and Nix, 1999), while Ge or Ge-rich SiGe islands are often not well organized (Abstreiter et al., 1996). In particular, Dorsch et al. (1998B) observed surface ripples aligned in the <100> directions at the early stage and a transition to islands well aligned in the same directions, similar to the simulated evolution sequence in Fig. 6.

For the Si(111) substrate (Fig. 7), the early-stage evolution shows similar surface patterns as that for isotropic systems, with shallow ridges and grooves in all directions. After a long-time evolution, however, discrete islands form and self-organize into a triangular array, unlike the isotropic system (Pang and Huang, 2006). Again, the triangular lattice of the cubic

crystal on the (111) plane is replicated on the surface at a larger scale. It is noted that, although the elastic property is isotropic in the (111) plane, the overall elastic property is still anisotropic and the anisotropic effect manifests over long time evolution. A few experimental studies have reported growth of Ge islands on Si (111) (Voigtlander and Zinner, 1993; LeGoues et al., 1996; Shklyaev et al., 1998). It was pointed out that the nucleation and growth of Ge islands strongly depend on the direction of surface steps on Si(111), a non-continuum feature beyond the scope of the current model. Nevertheless, the observed triangular or tetrahedral islands seem to exhibit similar symmetry as the triangular array in Fig. 7.

Numerical simulation shows that, for Ge on Si(110) (Fig. 8), the film surface evolves from parallel ripples to self-assembled lines in the [001] direction, consistent with the prediction by the linear analysis (Fig. 2c). To our knowledge, very few experimental observations have been reported for epitaxial surface evolution of SiGe or Ge films on Si(110). Arai et al. (1997) observed large Ge islands on Si(110), and Ferrandis and Vescan (2002) reported a monomodal size distribution of dome shaped Ge islands. Due to the fact that atoms on {110} surfaces are arranged in a rather complex manner (Vescan, 2002), further investigations with combined modeling and experimental efforts are necessary to understand the evolution dynamics of epitaxial surfaces on Si(110).

To further explore the anisotropic effect, high-index Si substrates have been used to grow Ge nanostructures (Omi and Ogino, 1999; Zhu et al., 1999). In particular, Si(113) surface belongs to a group of high-index surfaces with a rather small surface energy and was found to be thermally stable (Vescan, 2002). Figure 9 shows the simulated surface evolution process of

Ge on Si (113). As predicted by the linear analysis (Fig. 2d), the ripples at the early stage are aligned along two equivalent directions with angles $\pm 31^\circ$ off the $[\bar{1}10]$ direction. The surface ripples then evolve into discrete islands well organized in a diamond pattern. Due to the fact that the (113) plane is anisotropic, each island has an elliptic base as opposed to the circular islands on Si(001) and Si(111). Experimental observation of similarly elongated Ge islands on Si(113) was reported (Zhu et al., 1999).

Furthermore, it is found that the surface pattern depends on the mean film thickness. Figure 10 shows the surface patterns from numerical simulations after long-time evolution of Ge films on Si(001) substrates. When the mean film thickness is slightly above the critical thickness ($h_0 = 1.1h_c$), the islands form a cubic array. As the film thickness increases, the island array first becomes denser ($h_0 = 1.2h_c$) and then forms connected ridges ($h_0 = 1.4h_c$). Further increase of the mean film thickness leads to a surface pattern with perpendicular lines in the <100> directions ($h_0 = 1.5h_c$). Similar transition of the surface pattern from dots to lines has been observed experimentally (Gray et al., 2005). Similarly, on Si(113) substrates, increasing the mean film thickness leads to a transition from the organized island array to a line-shaped pattern (Fig. 11). A few experiments have observed wire-shaped Ge islands on Si (113) (Omi and Ogino, 1999). However, the observed Ge islands are elongated along the $[\bar{3}\bar{3}2]$ direction, while the simulated line patterns in Fig. 11 are aligned along two directions of angles $\pm 31^\circ$ off the $[\bar{1}10]$ direction. The discrepancy in the alignment suggests that, in addition to the elastic anisotropy, possible contributions on the pattern evolution dynamics from other physical origins (e.g., surface steps) not accounted for in the present model may be important for the high-index surfaces.

7. Concluding Remarks

In summary, we have developed a nonlinear model for surface evolution of epitaxial thin films on generally anisotropic crystal substrates. The effects of elastic anisotropy on surface patterns are elucidated by considering specific epitaxial systems, namely, Ge or SiGe films on Si substrates with four different surface orientations. Both the early-stage evolution as predicted by a linear analysis and the long-time evolution by numerical simulations clearly show specific ordering of the surface patterns under the influence of elastic anisotropy, contrasting the predictions by the isotropic models.

In addition to the elastic anisotropy considered in the present study, surface anisotropy can be important for understanding the dynamics of surface evolution. The present model can be readily extended to account for the effects of anisotropic surface diffusion and anisotropic surface energy. Furthermore, discrete surface steps play important roles for epitaxial growth on some substrate surfaces, e.g., Si(111) and Si(113). Further studies may adopt a continuum description of the stepped crystal surfaces (Shenoy and Freund, 2002) or incorporate dynamics of discrete steps (Yoon et al., 2007).

Acknowledgment

The authors gratefully acknowledge funding of this work by the US Department of Energy through Grant No. DE-FG02-05ER46230.

Appendix A. Solution to generally anisotropic, linear elastic half-space problems

Consider a semi-infinite half space subject to arbitrary tractions on the planar surface.

For isotropic, linear elastic solids, the solution can be derived from the solutions to the classical Cerruti's and Boussinesq's problems (Pang and Huang, 2006). For a generally anisotropic elastic solid, the following procedures are used in the present study to obtain a semi-analytical solution. Similar procedures have been used previously for cubic crystals (e.g., Lu and Suo, 2002).

In terms of displacements, the equilibrium equation for a linear elastic solid can be written as

$$C_{ijkl}u_{k,jl} = 0\,, \tag{A.1}$$

where C_{ijkl} is the elastic moduli and u_k the displacements, with the subscripts taking values from 1 to 3 for the Cartesian coordinates.

For the half-space problem with the x_3 axis normal to the surface, taking a Fourier transform of Eq. (A.1) with respect to the x_1 and x_2 coordinates, we obtain that

$$L_{ij}\frac{\partial^2 \hat{u}_j}{\partial x_3^2} + ikM_{ij}\frac{\partial \hat{u}_j}{\partial x_3} - k^2 N_{ij}\hat{u}_j = 0\,, \tag{A.2}$$

where

$$\hat{u}_j(x_3, k_1, k_2) = \frac{1}{2\pi}\int_{-\infty}^{\infty}\int_{-\infty}^{\infty} u_j(x_1, x_2, x_3)\exp(ik_1x_1 + ik_2x_2)dx_1dx_2\,, \tag{A.3}$$

$$\left[L_{ij}\right] = \begin{bmatrix} C_{55} & C_{45} & C_{35} \\ C_{45} & C_{44} & C_{34} \\ C_{35} & C_{34} & C_{33} \end{bmatrix}, \tag{A.4}$$

$$\left[M_{ij}\right] = \frac{1}{k}\begin{bmatrix} 2(k_1C_{15}+k_2C_{56}) & k_1(C_{56}+C_{14})+k_2(C_{25}+C_{46}) & k_1(C_{13}+C_{55})+k_2(C_{45}+C_{36}) \\ & 2(k_1C_{46}+k_2C_{24}) & k_1(C_{36}+C_{45})+k_2(C_{23}+C_{44}) \\ sym & & 2(k_1C_{35}+k_2C_{34}) \end{bmatrix}, \tag{A.5}$$

$$[N_{ij}] = \frac{1}{k^2}$$

$$\begin{bmatrix} k_1^2 C_{11} + 2k_1 k_2 C_{16} + k_2^2 C_{66} & k_1^2 C_{16} + k_1 k_2 (C_{12} + C_{66}) + k_2^2 C_{26} & k_1^2 C_{15} + k_1 k_2 (C_{14} + C_{56}) + k_2^2 C_{46} \\ & k_1^2 C_{66} + 2k_1 k_2 C_{26} + k_2^2 C_{22} & k_1^2 C_{56} + k_1 k_2 (C_{25} + C_{46}) + k_2^2 C_{24} \\ sym & & k_1^2 C_{55} + 2k_1 k_2 C_{45} + k_2^2 C_{44} \end{bmatrix}$$

(A.6)

and $k = \sqrt{k_1^2 + k_2^2}$. The Voigt's abbreviated notation for the elastic moduli has been used in Eqs. (A.4)-(A.6).

The solution to Eq. (A.2) takes the general form

$$\hat{u}_j = v_j(k_1, k_2) \exp(\lambda k x_3) . \tag{A.7}$$

Substituting (A.7) into Eq. (A.2) leads to

$$(\lambda^2 L_{ij} + i\lambda M_{ij} - N_{ij}) v_j = 0 . \tag{A.8}$$

Therefore, $v_j(k_1, k_2)$ can be determined as the eigen vector from Eq. (A.8) corresponding to the eigen value λ, which can be solved by setting the determinant of the coefficient matrix in (A.8) to be zero. In general, there exist six eigen values. For the half-space problem ($x_3 < 0$), however, the displacement necessarily vanishes as $x_3 \to -\infty$. Thus, the three eigen values with negative real part are discarded. With the remaining three eigen values, the complete solution takes the form

$$\hat{u}_j = \sum_{n=1}^{3} A_n v_j^{(n)} \exp(\lambda_n k x_3) . \tag{A.9}$$

Next, the boundary condition at the surface ($x_3 = 0$) is specified to determine the coefficients A_n. Using the displacement in (A.9), the strain and stress are obtained. Then, the surface tractions, $T_i(x_1, x_2) = \sigma_{3i}(x_1, x_2, 0)$, are obtained in terms of their Fourier transforms

$$\hat{T}_i = \sum_{n=1}^{3} D_i^{(n)} A_n , \tag{A.10}$$

where

$$D_i^{(n)} = \left(P_{ij} + k\lambda_n L_{ij}\right) v_j^{(n)}, \tag{A.11}$$

and

$$\left[P_{ij}\right] = \begin{bmatrix} ik_1C_{15} + ik_2C_{56} & ik_1C_{56} + ik_2C_{25} & ik_1C_{55} + ik_2C_{45} \\ ik_1C_{14} + ik_2C_{46} & ik_1C_{46} + ik_2C_{24} & ik_1C_{45} + ik_2C_{44} \\ ik_1C_{13} + ik_2C_{36} & ik_1C_{36} + ik_2C_{23} & ik_1C_{35} + ik_2C_{34} \end{bmatrix}. \tag{A.12}$$

Give the surface tractions, the coefficients A_n are then determined by Eq. (A.10). The Fourier transform of the surface displacement is then related to the surface traction by setting $x_3 = 0$ in Eq. (A.9), taking the form

$$\hat{u}_j(x_3 = 0; k_1, k_2) = Q_{ji}(k_1, k_2)\hat{T}_i, \tag{A.13}$$

where the coefficient matrix $Q_{ji}(k_1, k_2) = \sum_{n=1}^{3} v_j^{(n)} \overline{D}_i^{(n)}$, and $\overline{D}_i^{(n)}$ is the inverse of $D_i^{(n)}$ by the definition $\sum_{n=1}^{3} D_i^{(n)} \overline{D}_j^{(n)} = \delta_{ij}$. Consequently, the matrix $Q_{ji}(k_1, k_2)$ characterizes the compliance of the elastic half space, independent of the surface traction.

By the kinematic relation between displacement and strain, we obtain the Fourier transforms of the strain components

$$\hat{\varepsilon}_{\alpha\beta} = \frac{1}{2}\left(ik_\alpha \hat{u}_\beta + ik_\beta \hat{u}_\alpha\right) = \frac{1}{2}\sum_{n=1}^{3}\left(ik_\alpha v_\beta^{(n)} + ik_\beta v_\alpha^{(n)}\right) A_n \exp(\lambda_n k x_3), \tag{A.14}$$

$$\hat{\varepsilon}_{3\alpha} = \frac{1}{2}\left(ik_\alpha \hat{u}_3 + \frac{\partial \hat{u}_\alpha}{\partial x_3}\right) = \frac{1}{2}\sum_{n=1}^{3}\left(ik_\alpha v_3^{(n)} + \lambda_n k v_\alpha^{(n)}\right) A_n \exp(\lambda_n k x_3), \tag{A.15}$$

$$\hat{\varepsilon}_{33} = \frac{\partial \hat{u}_3}{\partial x_3} = \sum_{n=1}^{3} A_n \lambda_n k v_3^{(n)} \exp(\lambda_n k x_3). \tag{A.16}$$

Finally, the stress components are obtained by Hooke's law:

$$\hat{\sigma}_{ij} = ik_\beta C_{ij\alpha\beta}\hat{u}_\alpha + C_{ij\alpha 3}\left(\frac{\partial \hat{u}_\alpha}{\partial x_3} + ik_\alpha \hat{u}_3\right) + C_{ij33}\frac{\partial \hat{u}_3}{\partial x_3}. \tag{A.17}$$

As a special case for the general solution, consider a half space of a cubic crystal with its surface parallel to the (001) plane. In this case, the eigenvalue problem in (A.8) reduces to that in Lu and Suo (2002). The eigenvalues can then be obtained by solving a cubic algebraic equation of λ^2:

$$\lambda^6 + d_1\lambda^4 + d_2\lambda^2 + d_3 = 0\,, \tag{A.18}$$

where

$$d_1 = -\frac{R^2 + RS + S^2 - 1}{RS}, \tag{A.19}$$

$$d_2 = \frac{R^2 + RS + S^2 - 1}{RS} + \frac{S^3 - 2RS^2 + R^2S - 3S + 2R + 2}{R^2S}\frac{k_1^2k_2^2}{k^4}, \tag{A.20}$$

$$d_3 = -\frac{(R-S)^2 - 1}{RS}\frac{k_1^2k_2^2}{k^4} - 1, \tag{A.21}$$

with $R = C_{44}/(C_{12} + C_{44})$ and $S = C_{11}/(C_{12} + C_{44})$.

Furthermore, for an isotropic solid, we have $S - R = 1$, by which Eq. (A.18) becomes

$$\left(\lambda^2 - 1\right)^3 = 0\,. \tag{A.22}$$

This is a degenerated eigen value problem, with only one eigen value as the triple root: $\lambda = 1$. This would cause difficulty in the above solution procedure as we cannot find three linearly independent eigenvectors. The difficulty can be resolved by considering a different form of the solution instead of (A.7), namely

$$\hat{u}_j = \left(A_j + B_j k x_3\right)\exp(k x_3)\,. \tag{A.23}$$

Substituting (A.23) into Eq. (A.2) together with the isotropic elastic moduli (E and ν for the Young's modulus and Poisson's ratio, respectively), we obtain that

$$\frac{B_1}{k_1} = \frac{B_2}{k_2}\,. \tag{A.24}$$

$$A_3 = \frac{1}{k}\left(-ik_1 A_1 - ik_2 A_2 - (3-4\nu)\frac{k^2}{ik_1} B_1 \right), \tag{A.25}$$

$$B_3 = -\frac{ik}{k_1} B_1 . \tag{A.26}$$

Applying the boundary condition at the surface leads to three more equations that complete the solution. It is confirmed that this approach recovers the relationship between the surface tractions, $\hat{T}_i(k_1, k_2)$, and the surface displacements, $\hat{u}_j(x_3 = 0; k_1, k_2)$, obtained previously (Pang and Huang, 2006) by integrating the solutions to the classical Cerruti's and Boussinesq's problems for an isotropic, linear elastic half space.

Appendix B. Transformation of anisotropic elastic moduli

Let C_{ijkl} be the elastic moduli at the natural crystalline coordinate (x'_i in Figure 1). In an arbitrarily rotated coordinates (e.g., x_i in Figure 1 for the epitaxial system), the elastic moduli $\tilde{C}_{ijkl}$ can be obtained by transformation

$$\tilde{C}_{ijkl} = T_{im} T_{jn} T_{kp} T_{lq} C_{mnpq}, \tag{B.1}$$

where T_{ij} is the rotation matrix from the reference coordinates x'_i to the epitaxial coordinates x_i. For cubic crystals such as Si and Ge, the transformation equation reduces to

$$\tilde{C}_{ijkl} = C_{ijkl} - C_0 \left[\sum_{n=1}^{3} T_{in} T_{jn} T_{kn} T_{\ln} - \delta_{ij}\delta_{kl}\delta_{ik} \right], \tag{B.2}$$

where $C_0 = C_{11} - C_{12} - 2C_{44}$ and no summation is implied for indices *i* and *k*.

References

Abstreiter, G., Schittenhelm, P., Engel, C., Silveira, E., Zrenner, A., Meertens, D., Jager, W., 1996. Growth and characterization of self-assembled Ge-rich islands on Si. Semicond. Sci. Technol. 11, 1521-1528.

Asaro, R.J., Tiller, W.A., 1972. Interface morphology development during stress corrosion cracking: Part I. Via surface diffusion. Metall. Trans. 3, 1789-1796.

Arai, J., Ohga, A., Hattori, T., Usami, N., Shiraki, Y., 1997. Optical investigation of growth mode of Ge thin films on Si(110) substrates. Appl. Phys. Lett. 71, 785-787.

Brunner, K., 2002. Si/Ge nanostructures. Reports on Progress in Physics 65, 27-72.

Caro, L.D., and Tapfer, L., 1993. Elastic lattice deformation of semiconductor heterostructures grown on arbitrarily oriented substrate surfaces. Phys. Rev. B 48, 2298-2303.

Chiu, C., 1999. The self-assembly of uniform heteroepitaxial islands. Appl. Phys. Lett. 75, 3473-3475.

Cullis, A.G., Robbins, D.J., Barnett, S.J., Pidduck, A.J., 1994. Growth ripples upon strained SiGe epitaxial layers on Si and misfit dislocation interactions. J. Vac. Sci. Tech. A12, 1924-1931.

Dorsch, W., Strunk, H.P., Wawra, H., Wagner, G., Groenen, J., Carles, R., 1998A. Strain-induced island scaling during $Si_{1-x}Ge_x$ heteroepitaxy. Appl. Phys. Lett. 72, 179-181.

Dorsch, W., Steiner, B., Albrecht, M., Strunk, H.P., Wawra, H., Wagner, G., 1998B. The transition from ripples to islands in strained heteroepitaxial growth under low driving forces. J. Crystal Growth 183, 305-310.

Eaglesham, D.J., Cerullo, M., 1990. Dislocation-free Stranski-Krastanow growth of Ge on Si(100). Phys. Rev. Lett. 64, 1943-1946.

Ferrandis, P., Vescan, L., 2002. Growth and characterization of Ge islands on Si(110). Materials Sci. Eng. B89, 171-175.

Fitzgerald, E. A., 1995. GeSi/Si Nanostructures. Annu. Rev. Mater. Sci. 25, 417-454.

Floro, J.A., Chason, E., Freund, L.B., Twesten, R.D., Hwang, R.Q., Lucadamo, G.A., 1999. Evolution of coherent islands in $Si_{1-x}Ge_x$/Si(001). Phys. Rev. B 59, 1990-1998.

Freund, L.B., Suresh, S., 2003. Thin film materials: stress, defect formation, and surface evolution. Cambridge Univeristy Press, Cambridge, New York.

Gao, H., Nix, W.D., 1999. Surface roughening of heteroepitaxial thin films. Annu. Rev. Mater. Sci. 29, 173-209.

Golovin, A.A., Davis, S.H., Voorhees, P.W., 2003. Self-organization of quantum dots in epitaxially strained solid films. Phys. Rev. E 68, 056203.

Gray, J.L., Hull, R., Lam, C., Sutter, P., Means, J., Floro, J.A., 2005. Beyond the heteroepitaxial quantum dot: Self-assembling complex nanostructures controlled by strain and growth kinetics. Phys. Rev. B 72, 155323.

Grinfeld, M.A., 1986. Instability of the separation boundary between a non-hydrostatically stressed elastic body and a melt. Sov. Phys. Dokl. 31, 831-834.

Huang, R., Im, S.H. Im, 2006. Dynamics of wrinkle growth and coarsening in stressed thin films. Physical Review E 74, 026214.

Jesson, D.E., Chen, K.M., Pennycook, S.J., Thundat, T., Warmack, R.J., 1997. Mechanisms of strain induced roughening and dislocation multiplication in SiGe thin films. J.

Electronic Materials 26, 1039-1047.

Kassner, K., Misbah, C., Muller, J., Kappey, J., Kohlert, P., 2001. Phase-field modeling of stress-induced instabilities. Phys. Rev. E 63, 036117.

Kukta, R.V., Freund, L.B., 1997. Minumum energy configuration of epitaxial material clusters on a lattice-mismatched substrate. J. Mech. Phys. Solids. 45, 1835-1860.

Lam, C.-H., Lee, C.-K., Sander, L.M., 2002. Competing roughening mechanisms in strained heteroepitaxy: a fast kinetic Monte Carlo study. Phys. Rev. Lett. 89, 216102.

LeGoues, F.K., Hammar, M., Reuter, M.C., Tromp, R.M., 1996. In situ TEM study of the growth of Ge on Si(111). Surface Science 349, 249-266.

Liu, P., Zhang, Y.W., Lu, C., 2006. Anisotropy effect on heteroepitaxial growth of self-assembled islands. Appl. Phys. Lett. 88, 041922.

Lu, W., Suo, Z., 2002. Symmetry breaking in self-assembled monolayers on solid surfaces. II. Anisotropic substrate elasticity. Phys. Rev. B 65, 205418.

Medeiros-Ribeiro, G., Bratkovski, A.M., Kamins, T.I., Ohlberg, D.A.A., Williams, R.S., 1998. Shape transition of Germanium nanocrystals on a Silicon (001) surface from pyramids to domes. Science. 279, 353-355.

Meixner, M., Scholl, E., Schmidbauer, M., Raidt, H., Kohler, R., 2001. Formation of island chains in SiGe/Si heteroepitaxy by elastic anisotropy. Phys. Rev. B 64, 245307.

Ni, Y., He, L.H., Soh, A.K., 2005. Three-dimensional phase field simulation for surface roughening of heteroepitaxial films with elastic anisotropy. J. Crystal Growth 284, 281-292.

Omi, H., Ogino, T., 1999. Self-organization of Ge islands on high-index Si substrates. Phys.

Rev. B 59, 7521-7528.

Osten, H.J., Zeindl, H.P., Bugiel, E., 1994. Considerations about the critical thickness for pseudomorphic Si1-xGex growth on Si(001). J. Crystal Growth 143, 194-199.

Pang, Y., Huang, R., 2006. Nonlinear effect of stress and wetting on surface evolution in epitaxial thin films. Physical Review B 74, 075413.

Pang, Y., Huang, R., 2007. Bifurcation of surface pattern in epitaxial thin films under anisotropic stresses. J. Applied Physics 101, 023519.

Ross, F.M., Tromp, R.M., Reuter, M.C., 1999. Transition states between pyramids and domes during Ge/Si island growth. Science 286, 1931-1934.

Savina, T.V., Golovin, A.A., Davis, S.H., Nepomnyashchy, A.A., Voorhees, P.W., 2003. Faceting of a growing crystal surface by surface diffusion. Phys. Rev. E 67, 021606.

Savina, T.V., Voorhees, P.W., Davis, S.H., 2004. The effect of surface stress and wetting layers on morphological instability in epitaxially strained films. J. Appl. Phys. 96, 3127-3133.

Seol, D.J., Hu, S.Y., Liu, Z.K., Chen, L.Q., Kim, S.G., Oh, K.H., 2005. Phase-field modeling of stress-induced surface instabilities in heteroepitaxial thin films. J. Appl. Phys. 98, 044910.

Shenoy, V.B., Freund, L.B., 2002. A continuum description of the energetics and evolution of stepped surfaces in strained nanostructures. J. Mech. Phys. Solids 50, 1817-1841.

Shklyaev, A.A., Shibata, M., Ichikawa, M., 1998. Ge islands on Si(111) at coverages near the transition from two-dimensional to three-dimensional growth. Surface Science 416, 192-199.

Spencer, B.J., 1999. Asymptotic derivation of the glued-wetting-layer model and contact-angle condition for Stranski-Krastanov islands. Phys. Rev. B 59, 2011-2017.

Spencer, B.J., Davis, S.H., Voorhees, P.W., 1993. Morphological instability in epitaxially strained dislocation-free solid films: nonlinear evolution. Phys. Rev. B 47, 9760-9777.

Srolovitz, D.J., 1989. On the stability of surfaces of stressed solids. Acta Metall. 37, 621-625.

Stekolnikov, A.A., Furthmuller, J., Bechstedt, F., 2002. Absolute surface energies of group-IV semiconductors: dependence on orientation and reconstruction. Phys. Rev. B 65, 115318.

Stekolnikov, A.A., Furthmuller, J., Bechstedt, F., 2003. Adatoms, dimmers, and interstitials on group-IV (113) surfaces: first-principles studies of energetical, structural, and electronic properties. Phys. Rev. B 67, 195332.

Tekalign, W.T., Spencer, B.J., 2004. Evolution equation for a thin epitaxial film on a deformable substrate. J. Appl. Phys. 96, 5505-5512.

Vescan, L., 2002. Ge nanostructures grown by self-assembly: influence of substrate orientation. J. of Physics: Condensed Matter 14, 8235-8252.

Voigtlander, B., Zinner, A., 1993. Simultaneous molecular beam epitaxy growth and scanning tunneling microscopy imaging during Ge/Si epitaxy. Appl. Phys. Lett. 63, 3055-3057.

Yoon, M., Lee, H.N., Hong, W., Christen, H.M., Zhang, Z., Suo, Z., 2007. Dynamics of step bunching in heteroepitaxial growth on vicinal substrates. Physical Review Letters 99, 055503.

Zhang, Y.W., Bower, A.F., 1999. Numerical simulations of island formation in a coherent strained epitaxial thin film system. J. Mech. Phys. Solids 47, 2273-2297.

Zhang, Y.W., Bower, A.F., 2001. Three-dimensional analysis of shape transitions in

strained-heteroepitaxial islands. Appl. Phys. Lett. 78, 2706-2708.

Zhu, R., Pan, E., Chung, P.W., 2007. Fast multiscale kinetic Monte Carlo simulations of three-dimensional quantum dot islands. Phys. Rev. B 75, 205339.

Zhu, J., Miesner, C., Brunner, K., Abstreiter, G., 1999. Strain relaxation of faceted Ge islands on Si(113). Appl. Phys. Lett. 75, 2395-2397.

Table I. Elastic moduli and surface energy density of Si and Ge.

		Si	Ge
Elastic moduli (GPa)	C_{11}	166.2	128.4
	C_{12}	64.4	48.2
	C_{44}	79.8	66.7
Surface energy density (J/m^2)	(001)	2.39	1.71
	(111)	1.82	1.32
	(110)	2.04	1.51
	(113)	2.21	1.61

Figures

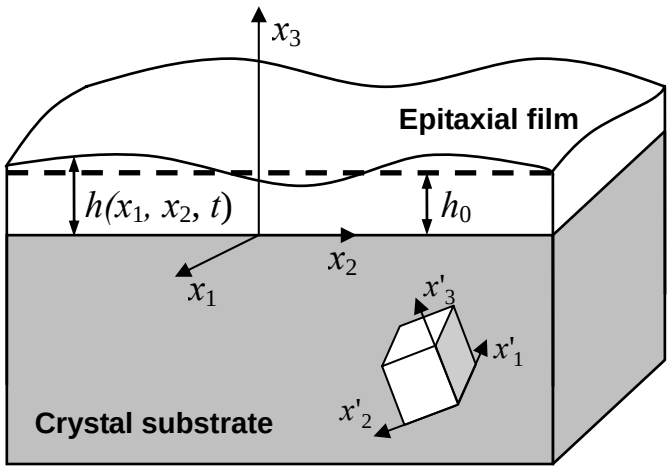

Figure 1. Schematic illustration of an epitaxial film on a crystal substrate.

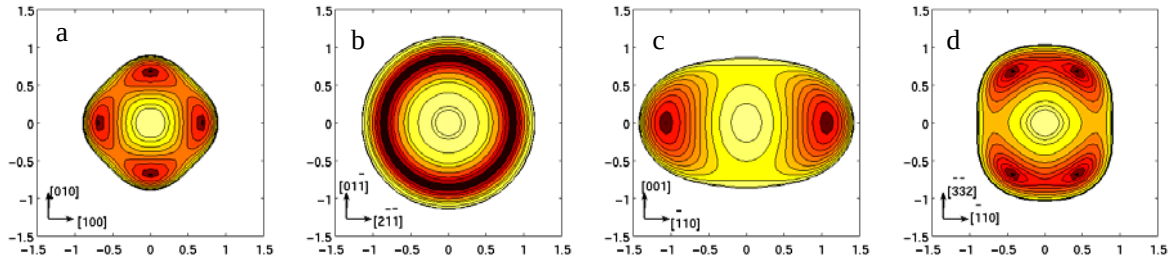

Figure 2. Contour plots of the initial growth rate for surface evolution of epitaxial Ge films ($h_0 = 0.2L$) on Si substrates of different surface orientations: (a) Si(001), (b) Si(111), (c) Si(110), and (d) Si(113).

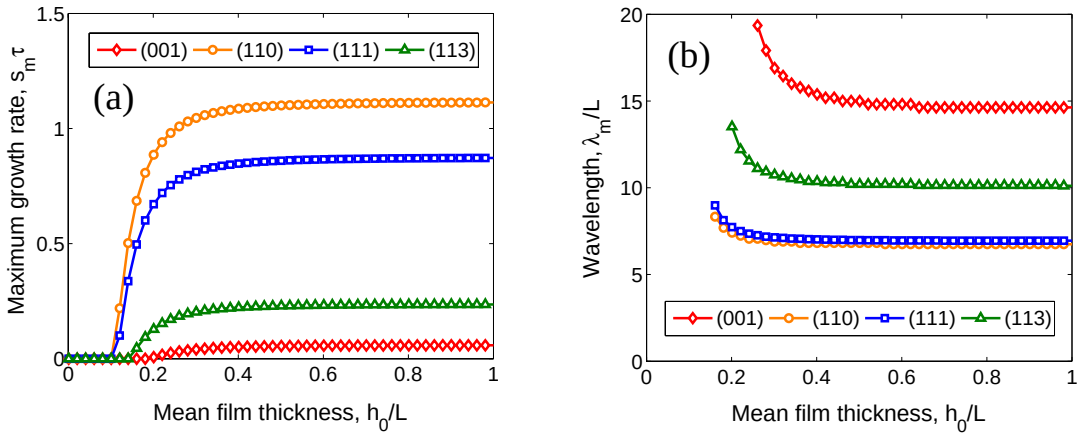

Figure 3. (a) The maximum initial growth rate and (b) the corresponding wavelength versus the mean film thickness for Ge films on Si substrates of different surface orientations.

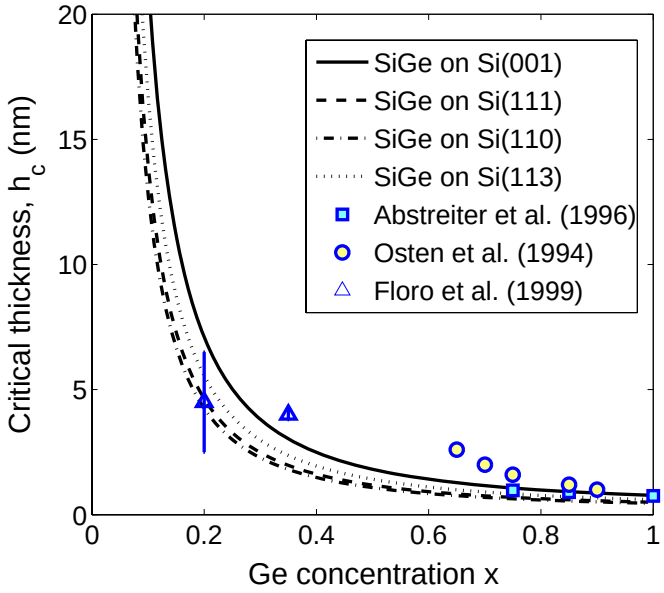

Figure 4. The critical thickness for SiGe films on Si substrates, as a function of Ge concentration.

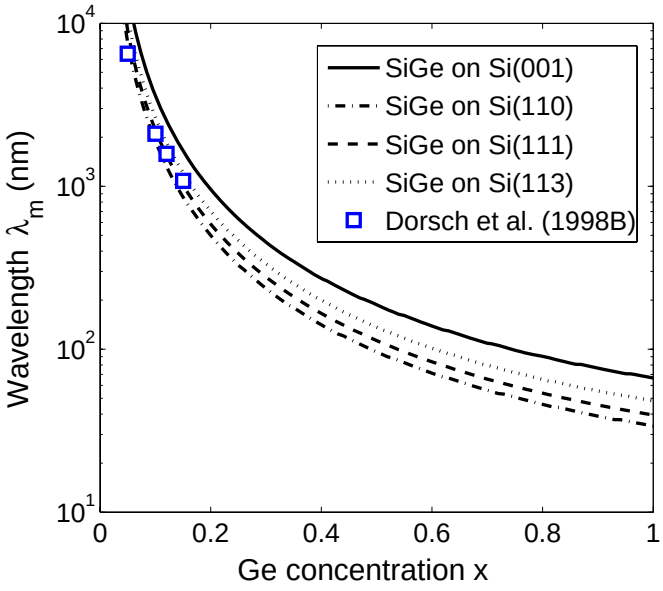

Figure 5. The wavelength corresponding to the fastest initial growth rate as a function of Ge concentration for SiGe films on Si substrates.

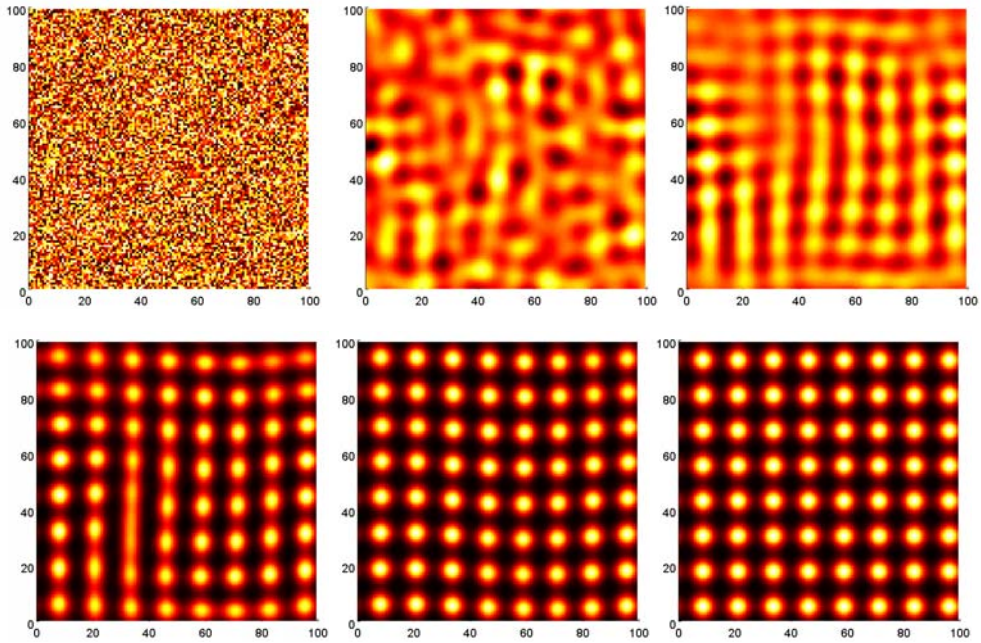

Figure 6. Simulated evolution of surface pattern for an epitaxial Ge film on a Si (001) substrate. First row: t = 0, 100, 500; second row: t = 1000, 2000, 10000.

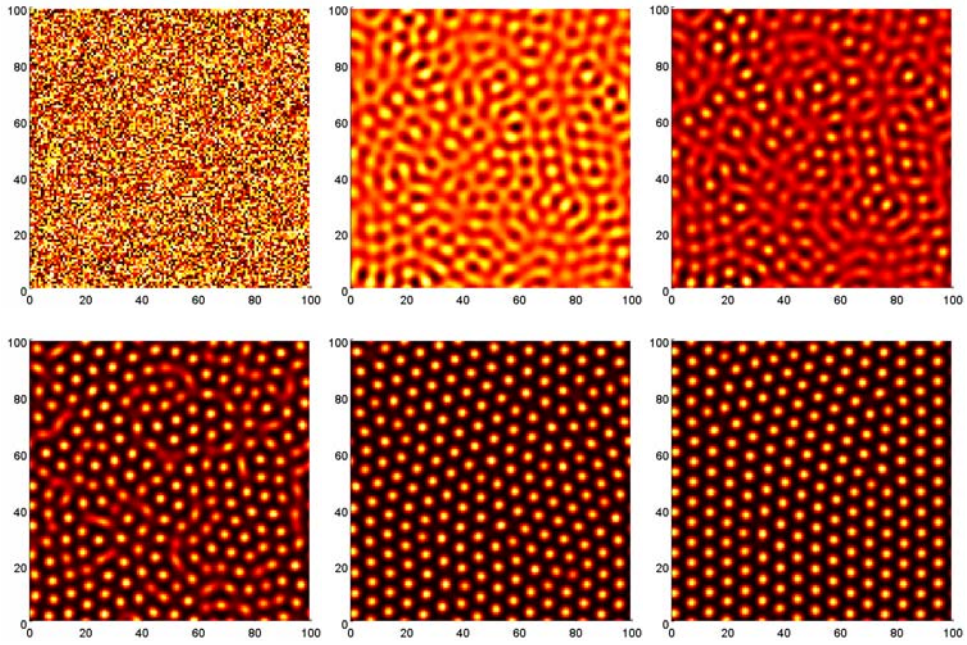

Figure 7. Simulated evolution of surface pattern for an epitaxial Ge film on a Si (111) substrate. First row: t = 0, 50, 80; second row: t = 100, 500, 10000.

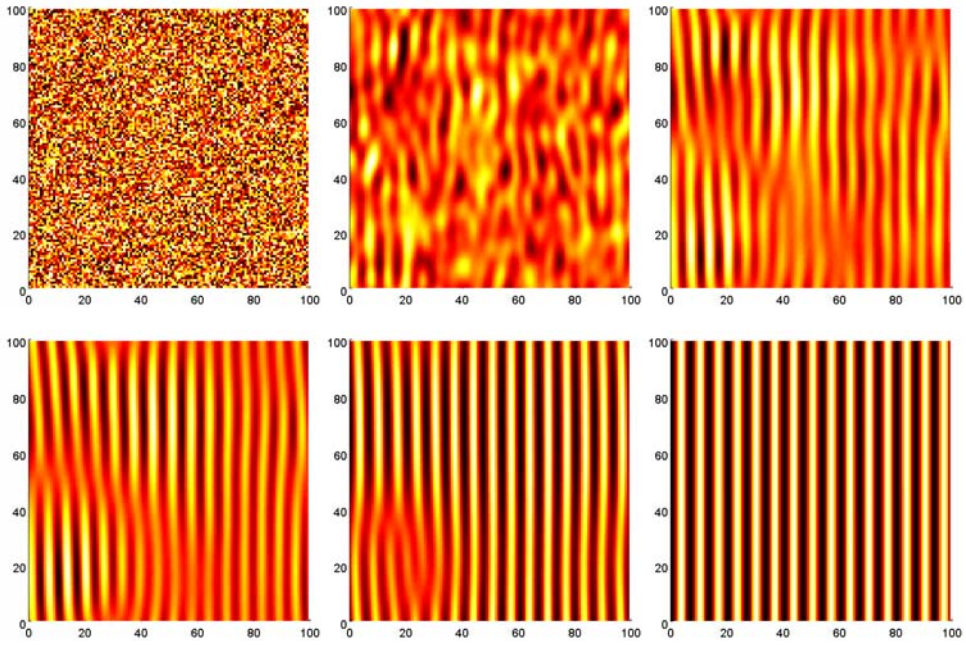

Figure 8. Simulated evolution of surface pattern for an epitaxial Ge film on a Si (110) substrate. First row: t = 0, 10, 50; second row: t = 100, 500, 1000.

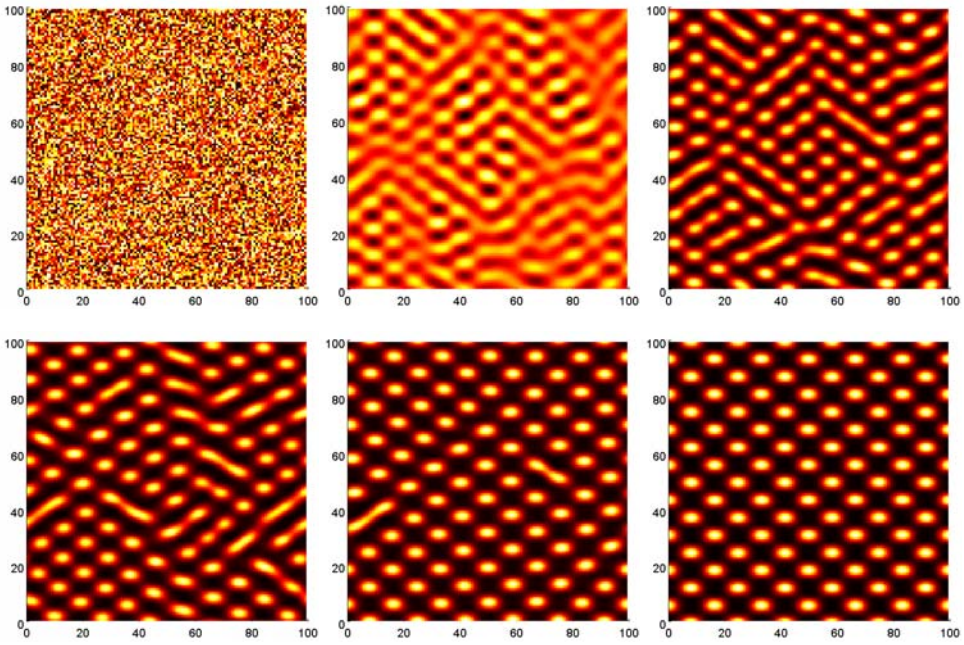

Figure 9. Simulated evolution of surface pattern for an epitaxial Ge film on a Si (113) substrate. First row: t = 0, 100, 200; second row: t = 500, 5000, 10000.

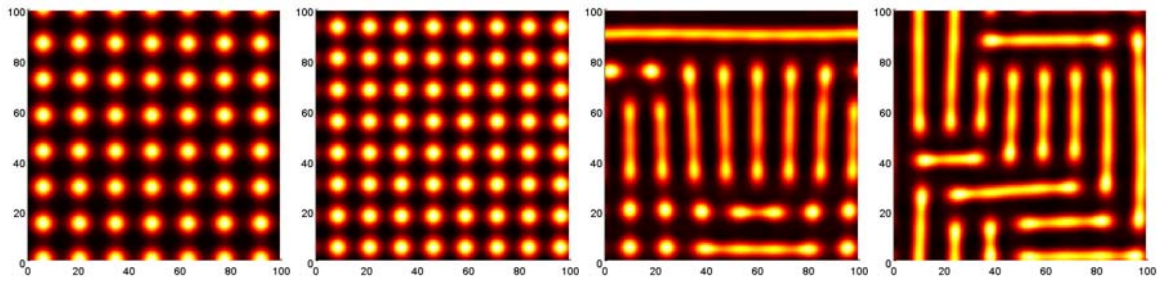

Figure 10. Transition of surface patterns for epitaxial Ge films on Si (001) substrates, with increasing mean film thickness. From left to right: $h_0 = 1.1h_c$, $h_0 = 1.2h_c$, $h_0 = 1.4h_c$, and $h_0 = 1.5h_c$.

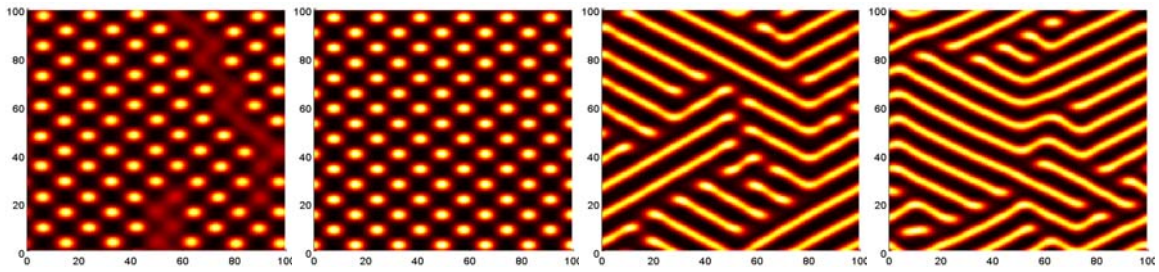

Figure 11. Transition of surface patterns for epitaxial Ge films on Si (113) substrates, with increasing mean film thickness. From left to right: $h_0 = 1.05h_c$, $h_0 = 1.1h_c$, $h_0 = 1.3h_c$, $h_0 = 1.5h_c$.